Contents lists available at ScienceDirect

Optical Materials

Laser materials based on transition metal ions

Richard Moncorgé

Centre de recherche sur les Ions, les Matériaux et la Photonique (CIMAP), UMR 6252 CEA-CNRS-ENSICaen, Université de Caen, 14050, Caen, France

ARTICLE INFO

ABSTRACT

The purpose of this presentation is to review the spectroscopic properties of the main laser materials based on transition metal ions which lead to noticeable laser performance at room temperature and, for very few cases, because of unique properties, when they are operated at cryogenic temperatures. The description also includes the materials which are currently being used as saturable absorbers for passive-Q-switching of a variety of other near- and mid-infrared solid state lasers. A substantial part of the article is devoted first to the description of the energy levels and of the absorption and emission transitions of the transition metal ions in various types of environments by using the well-known Tanabe-Sugano diagrams. It is shown in particular how these diagrams can be used along with other theoretical considerations to understand and describe the spectroscopic properties of ions sitting in crystal field environments of near-octahedral or near-tetrahedral symmetry. The second part is then dedicated to the description (positions and intensities) of the main absorption and emission features which characterize the different types of materials.

© 2016 Elsevier B.V. All rights reserved.

1. Introduction

There are two important categories of laser materials doped with transition metal ions of the ion group: those for which the active ions enter the crystals in sites of (near) octahedral symmetry and the optical transitions can be electric-dipole allowed vibronic transitions thanks to the coupling to odd phonon modes, and those having (near) tetrahedral symmetry sites and for which optical transitions can be electric-dipole allowed thanks to anti-symmetric components of the static crystal field. In the first case, the absorption and emission cross sections generally reach values between 10^{-21} and 10^{-19} cm^2 and the radiative lifetimes of the metastable emitting levels between a few tens of microseconds to a few milliseconds. In the second case, the optical transitions can be ten times more intense and the radiative emission lifetimes of the order of a few microseconds. The first category gathers all the most important near and mid-infrared laser materials based on Ti^{3+} (Ar3d^1), Cr^{3+} and V^{2+} (Ar3d^3), Co^{2+} (Ar3d^7) and Ni^{2+} (Ar3d^8) ions which have been studied in the past and exploited for their wide laser wavelength tunability or their ability to produce and/or to amplify ultra-short laser pulses. The second one also concerns a number of very important broad-band emitting laser materials such as those doped with Cr^{4+} (3 d^2), Cr^{2+} or Fe^{2+}, but also the same or different host materials doped again with Cr^{2+} or Cr^{4+} as well as with V^{3+}(3 d^2) or Co^{2+} (3 d^7) ions as saturable absorbers for passive Q-switching.

2. Generalities on the spectroscopic properties of transition metal ions

At room temperature, most of the transition-metal (TM) ion doped materials are broad-band absorbing and (eventually) emitting materials. There are however a few exceptions among which the famous ruby laser system (corundum Al$_2$O$_3$ doped with Cr^{3+}), the one indeed emits in the form of sharp lines (the famous ruby R lines) because of the strength of the crystal-field experienced by the Cr^{3+} laser active ions in this material.

Most of these materials are oxides and fluorides, but also, to a lesser extent, chlorides, selenides and sulfides single crystals and ceramics doped with TM ions of the Iron-group having the electronic configuration (Ar)3d^n with (Ar) = 1s^{2}2s^{2}2p^{6}3s^{2}3p^6, n = 1 to 10 and their atomic number Z is equal to 21 for Sc up to 30 for Zn. In contrast with trivalent rare-earth (RE) ions, the other important family of laser active ions, the 3 d optical electrons of these TM ions are the outermost electrons of the electronic configuration; they are not screened by any other electrons. Consequently, these 3 d electrons directly interact with the ligands, i.e. the negatively charged surrounding lattice ions, oxygen O^{2-} ions in the case of oxides, fluorine ions F$^-$ for fluorides, etc … The electronic energy levels thus experience a medium or strong ligand (or crystal) field, they eventually split into several components and the positions of the resulting crystal field energy levels for one particular ion strongly depend on the considered host material. Moreover, as the

optical electrons directly interact with the neighboring ions of the host lattice, the positions of their ligand field energy levels are very sensitive to the vibrations of these lattice ions. As a matter of fact, the energy levels of TM ions in solids are better described in terms of vibronic, i.e. electronic + vibrational, energy levels (like molecules), and the involved optical transitions which are generally spin-allowed and parity-forbidden transitions between the energy levels of the $3d^n$ electronic configuration, i.e. d-d transitions, are better described in terms of vibronic transitions. This is the reason why the optical absorption and emission spectra of most of the T.M. ion doped materials have the form of broad bands with widths of several hundreds of nanometers: over 400 nm in the case of $Ti^{3+}:Al_2O_3$ and 1200 nm in the case of $Cr^{2+}:ZnSe$, for instance.

Transition-metal ions of the Palladium-group having the $4d^n$ electronic configuration (with Z = 40 for Zr up to Z = 47 for Ag) or of the Platinum-group having the $5d^n$ configuration (with Z = 72 for Hf up to Z = 79 for Au) have never been lased so far in any host materials. These ions, when they are embedded in a crystal, experience a crystal field even stronger than in the case of the $3d^n$ ions. It means a stronger interaction with the surrounding host lattice ions, thus a stronger interaction with the lattice vibrations. This is resulting in wider optical bands and stronger non-radiative relaxation processes, thus strong excited-state absorption (ESA) losses and very reduced fluorescence quantum efficiencies, with emission lifetimes generally decreasing very significantly with the sample temperature.

No transition-metal ion doped amorphous material has ever led either to laser action. Several attempts have been made in the past and some researchers working with glass fibers still hope to achieve laser action with Cr^{3+} and Cr^{4+} dopants. The task however remains very tough since in amorphous materials, the optical transitions become even wider than in crystals, restricting further the wavelength domain within which there is no excited-state absorption (ESA) losses, and the transition cross-sections become even smaller than that found in crystals.

No transition-metal ion doped crystal, ceramic or amorphous material has ever lased in the near-UV and visible spectral domains. This is mainly due to the proximity of the energy levels and the non-radiative radiationless transitions between them, but also and mainly because of the strong electric-dipole allowed ESA bands (inter-configurational and charge-transfer optical transitions) which occur in the considered wavelength domains.

2.1. Tanabe-Sugano energy level diagrams

Without entering into the details, which can be found in many articles and reference books, let us focus here on the energy level diagrams as reported [1] by Tanabe and Sugano (TS). These diagrams were established within the framework of a point-charge model in the strong field approximation. Therefore, they do not account explicitly for effects such as covalency (as detailed for instance in Ref. [2]) and local site distortion. Although the calculation could be done rather easily, they do not include either the effect of spin-orbit coupling. Nevertheless, they remain very useful to roughly understand and to account for most of the spectroscopic properties of TM ions in any solid state environment. These diagrams can be found in many books [3]. The matrices which allow to build them, even by including spin-orbit coupling, can be found in the Griffith's book [4]. These TS energy level diagrams give the reduced energies E/B of the crystal-field levels of all the TM ions having the electronic configuration $(Ar)3d^n$ with $2 \leq n \leq 7$, as a function of the reduced quantity Dq/B; Dq measures the strength of the local crystal field supposed of octahedral symmetry and B stands for one of the Racah intra-ionic and electron-electron interaction parameters. The energy level diagrams for n = 1 and 9

are not reported because they are associated to one d electron or one hole, respectively, and their two-levels diagrams, are only made of the two energy states ^2E and $^2T_2$.

In fact, the calculations of these energy level positions are performed for each TM active ion, by accounting for the kinetic energies of the electrons and 3 types of interactions, (i) the Coulombic (attractive) interactions between the electrons and the nuclei of each active ion, with the Hamiltonian (including the kinetic energies) noted H_0, (ii) the Coulombic (repulsive) intra-ionic interactions between the electrons, with the Hamiltonian noted H_{ee}, and (iii) the electrostatic attractive interactions between the positively charged active ions and their neighboring ligands associated with the so-called ligand- (or crystal-) field Hamiltonian noted H_{cf}. Starting from that, two approaches have been used. In the medium field approach, the crystal field experienced by the TM active ions in the crystals is treated as a perturbation ($H_e \gg H_{ee} \gg H_{cf}$), the action of the first two interactions give rise to the "spectral terms" noted ^{2S+1}L, with the spin S and the angular momentum L, and the crystal field to the splitting of these spectral terms and the shifts of the resulting "Stark" components or "crystal-field terms" noted $^{2S+1}\Gamma$, where Γ stands for the irreducible representations associated with the crystallographic symmetry point group corresponding to the arrangement of the ligands immediately around the considered active ions. For example, in the case of the d^3 electronic configuration, the spectral term ^4F (which means that L = 3 and S = 3/2) gives rise to the 3 crystal-field energy terms, $^4A_2$, $^4T_2$ and $^4T_1$ (the latter being sometimes noted $^4T_{1F}$ or $^4T_1(^4F)$ to remember that it comes from the spectral term ^4F. In the strong field approximation, that used in fact by Tanabe and Sugano, the crystal field is assumed to be stronger than the inter-electronic interactions ($H_e \gg H_{cf} \gg H_{ee}$). Therefore, H_{cf} acts directly on the d orbitals and the d^n electronic configuration and splits them into t_2 and e crystal field orbitals and $t_2^m e^{n-m}$ electronic configurations with energies $E(t_2^m e^{n-m}) = (6n-10\ m)Dq$, prior to the inter-electronic Hamiltonian H_{ee} which then couples the electronic orbitals to form the same crystal field energy levels $^{2S+1}\Gamma$, as above. At the end, the two methods lead to the same energy level scheme with spectral terms on the left side and with crystal field terms and crystal-field electronic configurations on the right hand side.

It is worth noting here that in the TS diagrams, the positions of the crystal field energy levels have been all reported with respect to the lowest one, i.e. to the final fundamental state. This is the reason why, in the case of the d^3 electronic interaction, for instance, the $^4A_2$ energy level is reported with the same (assumed equal to zero) energy. Therefore, the energy E reported on the ordinate axis just represents the energy separation of each excited state with respect to the ground state. It is absolutely necessary to understand this point if one wishes to correctly understand more complicated situations like that found in the case of the d^4 configuration, for example. Indeed, in that case, above a Dq/B value of about 2.65, the $^3T_1$ excited state shifts down below the ^5E and replace it as fundamental state. Therefore, the reported energy curves above this Dq/B value are just obtained by adding the calculated energy of the ^5E.

As introduced above, the B parameter is one of the three Racah parameters (A, B and C) with which the energies of the spectral terms are calculated. The relations giving these energies versus these parameters can be found for instance in Ref. [5]. These three Racah parameters themselves can be derived from the three inter-electronic Slater integrals noted F_0, F_2 and F_4. In the TS diagrams, only one B parameter associated with each kind of configuration appears and is used as reduction factor for the energy and the crystal-field strength parameter reported on the axes of the diagrams. The reason for that is that for any ion associated with a particular electronic configuration all the energy levels have the

same dependence on the A parameter so that it disappears when energies, as just mentioned, are calculated and reported with respect to the fundamental one. Moreover, all the energy levels have been calculated by assuming a particular C/B. These free-ion B parameters and C/B ratios have been tabulated for each type of ions and valency state in Ref. [5] p 109. In practice, they are adjusted to experimental data, such as the positions of the main spin-allowed absorption bands, to account for covalency effects (overlap of active ion electronic orbitals with ligands' orbitals) and they are found smaller than their free-ion values (reduction of free-ion inter-electronic repulsion parameters often called "nephelauxetic" effect). These covalency effects generally increase (B and C decreasing values) when going from fluorides to oxides and selenides and along the series of ions Cr^{2+}, V^{2+}, Co^{2+}~ Ni^{2+}, Fe^{2+}, Cr^{3+} and V^{3+}. The value of the B parameter for the Cr^{3+} ion, for instance, is reduced from 920 cm^{-1} for the free ion down to 740 cm^{-1} in a fluoride like $LiCaAlF_6$ (colquirite) and to 640 cm^{-1} in Al_2O_3 (corundum or alumina).

As mentioned above, each TS energy level diagram was established for an octahedral environment with the corresponding parameter $Dq = Dq_{oct}$, and $Dq_{oct} \approx \frac{35Ze^2}{4a^5} \frac{2}{105} \langle r^4 \rangle_{3d}$, where a is the distance between the central ion and the ligands, Ze the effective charge of each ligand and $\langle r^4 \rangle_{3d}$ the standard radial integral calculated for the 3 d electrons. The same calculations can be done, however, for cubic and tetrahedral environments inscribed in the same cube, as reported in Fig. 2. From that different arrangements, it can be demonstrated that two other Dq parameters can be introduced, i.e. $Dq = Dq_{tetra} = -4/9 \ Dq_{oct}$ for a tetrahedral environment and $Dq = Dq_{cub} = -8/9 \ Dq_{oct}$ for a cubic one. It simply means that the average strength of a tetrahedral crystal-field is about half that of an octahedral one and about the same as found for a cubic one. The interesting consequence is that the TS diagrams can be also used to describe the energy levels of any TM ion in a (near) tetrahedral or cubic environment. This can be done, for instance, for a tetrahedral environment by consulting the diagram of the "complementary" electronic configuration and by looking at the energy levels corresponding to a Dq value equal to about 4/9 what it would be for an octahedral environment inscribed in the same cube. As there are 10 possible electrons on a 3 d electron shell, the complementary of an $(Ar)3d^n$ electronic configuration is (Ar) $3 d^{10-n}$. Therefore, for instance, the positions of the energy levels of a Cr^{4+} or a Mn^{5+} ion (3 d^2 configuration) in a tetrahedral environment will be given by the TS diagram for a 3 d^8 ion (Ni^{2+} for instance) in an octahedral crystal field. In the same way, the positions of the energy levels of a Co^{2+} ion (3 d^7) in a tetrahedral environment will be given by the TS diagram of Cr^{3+} (3 d^3) in an octahedral crystal field.

Last point but not the least, the TS energy level diagrams reveal the existence of more or less sensitive energy spacings between ground and excited states, thus, as we shall see in the following, of absorption and emission transitions having the form of sharp lines or of broad bands. Taking the previous case of Cr^{3+}(3 d^3) in an octahedral environment, it is shown for example that an energy level like the spin doublet ^2E remains approximately at the same position with respect to the $^4A_2$ spin-quartet ground level. It means that for materials like ruby for which the local crystal field corresponds to $Dq/B \geq 2.5$, the lowest excited energy level is this ^2E level and that the lowest $^2E \leftrightarrow {}^4A_2$ spin-forbidden ($\Delta S \neq 0$) absorption and emission transitions observed in this material will have the form of sharp lines, the famous ruby R lines already mentioned above. On the other hand, energy levels like $^4T_2$, $^4T_{1F}$ and $^4T_{1P}$ strongly vary with the crystal field. In this case, it indicates the existence of spin-allowed absorption transitions such as $^4A_2 \leftrightarrow {}^4T_2$ having the form of broad bands. In fact, the local slope of each calculated energy level versus the Dq crystal field strength

parameter can be used, within the framework of the single-configuration coordinate (SCC) model [6] which will be discussed in the next paragraph, to give an estimate of the width of each associated absorption band. The slopes and the positions of these highly sensitive excited energy levels also show in which material and for which crystal field, a broad band or a sharp line emission should be observed. According to the TS diagram for Cr^{3+}, it is clear that broad band emissions associated with $^4T_2 \rightarrow {}^4A_2$ (vibronic) optical transitions should be observed as soon as the Cr^{3+} ions are incorporated in sites with local crystal fields of medium and low strengths corresponding to Dq/B values below about 2.1. Indeed, in these situations (see in section 3b), the $^4T_2$ excited state becomes the lowest one or it can be thermally populated from the ^2E either at room temperature or, after heating, at the considered operating temperature.

2.2. Electron-phonon coupling, vibronic transitions and desexcitation rates

Because of the lattice vibrations, the crystal field experienced by a luminescent active ion will be the sum of two contributions, a static contribution, the one involved in the T.S. calculations, and a dynamic one which oscillates at the frequencies of the local and/or the lattice phonon modes. In other words, the strength of the resulting crystal field is modulated by the vibrations of the surrounding ions and, in the case of the T.M. ions, interaction of the $3d^n$ electrons with this modulated crystal field (so-called electron phonon coupling) will lead to a description of the energy levels in terms of potential (or configuration) curves. Within the framework of this description and the so-called single-configuration coordinate (SCC) model, each energy level is represented by a parabola centered around an equilibrium position of the ions (a generalized "normal" coordinate often noted Q_0) and, according to the theory, the relative shifts of the parabola associated with the different excited states will be proportional to the slopes $s_i = \frac{\partial E_{ei}}{\partial (Dq)}$ of the energies calculated versus the crystal field parameter Dq. Assuming the same phonon mode of energy $\hbar\omega$ in the ground- and the excited-states (linear electron-phonon coupling approximation) but different electron-phonon coupling strengths measured by the Huang & Rhys parameters S_g and S_{ei}, respectively, the shift $\delta Q_0^{ei} = Q_0^{ei} - Q_0^g$ of each parabola will be determined by using the following procedure: (1) determination of the energies of the intersection points of the excited-state parabola with the vertical axis $Q = Q_0^g$ by using the experimental positions of the absorption band maxima and by confronting them with the corresponding T.S. energy level diagram, this first step providing the Dq and B values of the considered system, (2) determination of the "Stokes shift" $\Delta E_S = (S_g + S_{e1})\hbar\omega$ measuring the energy separation between the maxima of the first absorption and emission bands, S_{e1} being the Huang & Rhys parameter for the first absorption band ($i = 1$), and determination of the associated equilibrium position $Q_0^{e1} = Q_0^g + \delta Q_0^{e1}$ (3) determination from the T.S. diagrams of the slopes s_i of each considered excited energy level i, and of the calibration factor K such as $S_{e1}\hbar\omega = Ks_1^2$ for $i = 1$, (4) determination of the equilibrium positions of the excited-state energy levels of interest by writing $\delta Q_0^{ei} = \frac{s_i}{s_1} \delta Q_0^{e1}$, then $S_{ei}\hbar\omega = Ks_i^2$. It is worth noting here that slopes can be positive or negative which means that potential curves can be displaced towards higher Q values, which corresponds to local lattice expansions, or towards lower Q values (level ^2E of Co^{2+}, d^7 electronic configuration for material with Dq/B < 2.2, for instance), corresponding then to lattice contractions.

Within the framework of this SCC model, a number of useful expressions can be derived to describe the band-shapes of the vibronic optical transitions but also their radiative and non-radiative properties versus temperature. To illustrate that matter,

we have used here the Struck & Fonger (S&F) approach. The transition rate associated with any particular desexcitation is written as the sum of two contributions

$$W = W_R + W_{NR} \tag{1}$$

or, in terms of lifetimes,

$$\frac{1}{\tau_F} = \frac{1}{\tau_R} + W_{NR}, \tag{2}$$

where τ_F stands for the fluorescence lifetime of a particular emitting level, τ_R for its purely radiative lifetime, and W_{NR} for any other non-radiative desexcitation rate. As a matter of fact, because of a strong electron-phonon coupling, non-radiative transitions caused by the transfer of electronic excitation into heat through the lattice vibrations represents one of the most important issues for materials doped with transition metal ions. They directly condition their fluorescence quantum efficiency $\eta = \frac{\tau_F}{\tau_R} = \frac{W_R}{W_R + W_{NR}}$ at a given temperature and their use as a laser system at that temperature.

- Non-radiative multiphonon relaxation processes and desexcitation rates

Restricting the discussion to non-radiative desexcitations caused by these lattice vibrations, two types of phonon modes are generally invoked, so-called "promoting" phonon modes inducing non-radiative transitions by mixing the vibrational wavefunctions of adjacent vibronic energy levels, and "accepting" phonon modes reflecting the overlap of the vibrational wavefunctions mediating the dissipation of the excitation energy in the crystal by involving a set of p phonons. In the case of transition metal ions, one generally invokes the latter with an energy noted $\hbar\omega_{accep}$ which roughly corresponds to a weighted average energy of all the vibrational modes which can be involved in the non-radiative desexcitation processes associated with a particular transition.

According to the S&F formalism, when the desexcitation process involves p phonons with $p \gg 2$, the associated non-radiative rate between two adjacent energy levels a and b at some temperature T transforms like:

$$W_{NR}^{ab} = N_{ab} W_p(S, \hbar\omega, T) \tag{3}$$

where N_{ab} is the electronic part of the transition process (of the order of 10^{13} s^{-1}) which depends on the mixing of the electronic and vibrational wavefunctions via the above mentioned promoting modes, and $W_p(S, \hbar\omega, T)$ is given by:

$$W_p(S, \hbar\omega, T) = e^{-S(2\overline{m}+1)}\left[\frac{1+\overline{m}}{\overline{m}}\right]^{p/2} I_p\left[2S(\overline{m}(\overline{m}+1))^{1/2}\right] \tag{4}$$

where S is the above defined Huang & Rhys parameter, I_p stands for a modified Bessel function of order p, and $\overline{m} = (e^{\hbar\omega/kT} - 1)^{-1}$ for the Bose-Einstein factor for the accepting modes. Then, it can be shown that, at very low temperature, $W_p(T)$ transforms like:

$$W_p(T = 0) = S^p \frac{e^{-S}}{p!} \tag{5}$$

which is the well-known Pekar formula.

From the detailed expression for W_{NR} [7] it is also possible to establish some selection rules on the symmetry of the promoting modes and their impact on the non-radiative transitions between particular energy levels. For instance, in the case of Cr^{3+} doped materials in which Cr^{3+} ions have a nearly octahedral environment,

their ground- and first excited-states $^4A_2$ and $^4T_2$ can interact only via promoting phonon modes of T_{1g} symmetry. On the other hand, for Co^{2+} ions in the same type of environment, their ground- and first excited-states $^4T_1$ and $^4T_2$ can be coupled by several phonon modes of T_{1g}, T_{2g} and E_g. It is thus expected that stronger non-radiative transitions occur in the case of Co^{2+} than in the case of Cr^{3+} doped materials. This generally manifests in stronger multi-phonon relaxations and lower fluorescence quantum efficiencies for the former compared to the latter.

Assuming a weak electron-phonon coupling and at low temperatures, the expression (4) can be advantageously reduced to the exponential form [7,8]:

$$W_p(T) = W_0 e^{-\alpha_{NR}\Delta E_{ab}} \tag{6}$$

with $\alpha_{NR} = [\ln(p/S) - 1]/\hbar\omega$ and where ΔE_{ab} stands for the energetic separation between levels a and b. The expression is known as the "energy gap law" (or tunneling effect induced non-radiative transitions law); it applies rather well to the case of rare-earth ions.

On the other hand, assuming a strong electron-phonon coupling, which more specifically applies for transition metal ions, and at high temperature, the expression (4) can be also reduced to the exponential form:

$$W_p(T) = W_0 e^{-\Delta E/kT} \tag{7}$$

where it is assumed that the non-radiative transitions can occur via thermal activation of the excited-state vibrational modes and the crossing point of the potential curves associated with the two considered electronic energy levels. ΔE_{ab} is the activation energy corresponding to the energy gap between the lowest vibrational level of the considered excited state and this crossing point.

- Vibronic transition rates, selection rules and band-shapes

According to the S&F formalism, in the case of vibronic transitions, the radiative part W_R of the transition rate which appears in the expression (1) can be treated in a similar way by writing:

$$W_R^{ab} = R_{ab} W_p(S, \hbar\omega, T) \tag{8}$$

where R_{ab} is proportional to the square of the considered vibronic transition matrix element (electric- or magnetic-dipole transition matrix element) and $W_p(T)$ is again defined by equation (4) but represents here the band-shape function of a vibronic transition associated with p phonons. It is worth noting, however, because of the different electron-phonon coupling mechanisms, that the vibrational accepting modes participating in the non-radiative transitions are not necessarily all the same as those participating in the vibronic band-shapes. In the case of Ni^{2+} (3 d^8 configuration), for instance, it is generally found that the energy of the accepting modes $\hbar\omega_{accep}$ which can be deduced from the thermal variations of the non-radiative transitions (as derived from the measured fluorescence decays) is smaller than that corresponding to the totally symmetric vibrational mode noted A_{1g} which is most often involved in the description of the vibronic band-shapes.

In the general case, at low temperatures, when the electron-phonon coupling is not too strong, thus when the potential curves for the energy levels are not too much displaced between each other and the associated Huang & Rhys parameters are not too high ($S \leq 5$), the vibronic transitions occur from the lowest vibrational state of the initial electronic energy levels to all the vibrational states of the final energy levels. In that situation, their band-shapes, as given by Expr. 5, often take the form of a sharp line corresponding to what is called a "zero-phonon" transition (p = 0 in

Expr. 5) flanked of a broad-band often called a "sideband" associated with the absorption or the emission of 1, 2, ...n phonons. Moreover, according to Expr. 5, the intensity ratio between the zero-phonon line and the zero-phonon line+ its associated vibronic sideband should be equal to $\frac{I_{00}}{I_{total}} = e^{-S}$. Such intensity ratio, when it is measurable, thus gives an estimate of the electron-phonon coupling strength parameter S.

Without entering into the detail of the expression for R_{ab}, a minimum should be said at this point on the underlying transition matrix elements and resulting selection rules to really understand the spectroscopy of the transition metal ions in a crystal, and more specifically, which is very important for many laser materials, when these ions site in centro-symmetric or non-centro-symmetric crystalline environments. Very briefly, the vibronic transitions between two electronic states a and b essentially depend on the square of matrix elements of the form $\langle \psi_b | \overrightarrow{P}_{eff} | \psi_a \rangle$ where $\overrightarrow{P}_{eff}$ is an effective transition operator which takes different forms depending on the nature and the parity of the initial and final electronic wavefunctions ψ_a and ψ_b: the form of an odd parity electric-dipole transition moment $\overrightarrow{D} = \sum e \overrightarrow{r}_i$ for different parity wavefunctions, or the form of an even parity magnetic-dipole transition moment $\overrightarrow{M} = \frac{e}{2mc}(\overrightarrow{L} + 2\overrightarrow{S})$ for same parity wavefunctions, knowing that parity is given by $P = (-1)^{\sum_i l_i}$ when l_i stands for the angular momentum of each optical electrons and that $l_i = 2$ for a d electron, and that a magnetic-dipole optical transition is generally much weaker than an electric-dipole one.

Namely, when the active ion sites in a centro-symmetric crystallographic site, such as a perfect or nearly perfect octahedral site, the initial and final wavefunctions have the same parity. In this case, to have a non-zero matrix element and to observe an optical transition, the effective transition operator $\overrightarrow{P}_{eff}$ must be of even parity. Therefore, if the observed transition is a purely (zero-phonon) electronic transition, this transition will be necessarily a magnetic-dipole allowed transition and the transition operator will be written $\overrightarrow{P}_{eff} = \overrightarrow{M}$. Nevertheless, if the considered transition is a vibronic (electronic + vibrational) transition, the operator will take the form:

$$\overrightarrow{P}_{eff} = \sum_i \frac{\overrightarrow{P}|\psi_i\rangle\langle\psi_i|V_q}{E_a - E_i} + c.c. \tag{9}$$

where $\overrightarrow{P}$ is the electric- or magnetic-dipole operator, V_q represents one of the possible phonon modes of the system and ψ_i the electronic wavefunction of an intermediate electronic state. In this case, the observed vibronic transition can be electric-dipole allowed $(\overrightarrow{P} = \overrightarrow{D})$ if the active phonon mode is an odd mode, T_{1u} for instance, but it can be magnetic-dipole $(\overrightarrow{P} = \overrightarrow{M})$ if the involved phonon mode is an even mode. In the first situation, it is said that the transition is a "forced" electric-dipole transition.

When the active ion sites in a non-centrosymmetric crystallographic site, such as a perfect or nearly perfect tetrahedral site, optical transitions can be directly electric-dipole allowed thanks to the anti-symmetric components V_{odd} of the static crystal field and the above transition operator transforms like:

$$\overrightarrow{P}_{eff} = \sum_i \frac{\overrightarrow{D}|\psi_i\rangle\langle\psi_i|V_{odd}}{E_a - E_i} + c.c. \tag{10}$$

This is a very important situation which is encountered in many modern laser materials (gain media as well as saturable absorbers) based on transition metal ions.

In the end, the radiative transitions being enabled thanks to the static as well as to the dynamic components of the crystal field, the vibronic radiative lifetime, as introduced in the expression (2) will

be generally equal to the sum of two terms:

$$\frac{1}{\tau_R} = \frac{1}{\tau_{stat}} + \frac{1}{\tau_{dyn}} \tag{11}$$

τ_{stat} having its origin in the purely static part of the crystal field, the one does not depend significantly on the temperature, and τ_{dyn} coming from the vibrational part, the one can depend on the temperature and varies according to the relation [9]:

$$\frac{1}{\tau_{dyn}(T)} = \frac{1}{\tau_{dyn}(T=0)} \coth\left(\frac{\hbar\omega_{enab}}{kT}\right) \tag{12}$$

where $\hbar\omega_{enab}$ stands for the phonon modes for which the vibronic term R_{ab} appearing above in Expr. (7) is different from zero. The energy $\hbar\omega_{enab}$ is generally equal to the weighted average energy associated with all the odd symmetry phonon modes (bending and stretching phonon modes noted T_{1u}, T_{2u} and T_{1u}') conducting to electric-dipole allowed vibronic transitions.

2.3. Excited-state absorption and charge-transfer bands

As introduced above, non-radiative transitions and fluorescence quantum efficiency at a given temperature are very important issues for laser materials based on transition metal ions. Another important one is excited-state absorption (ESA) and, to a lesser extent, charge transfer bands.

ESA in the case of rare-earth ions is often very detrimental for laser operation. There are however some circumstances for which ESA can be used to reach laser emission (up-conversion laser emission) from upper energy levels. In the case of transition metal ions, because ESA appear as broad bands and very few systems emit from excited energy levels other than the lowest one, it is always very detrimental. There is simply no laser operation when a particular ESA band coincides with the emission one or a narrowing of the laser emission spectrum and tunability due to a partial overlap of the ESA and emission bands. Many materials have been considered and deeply studied in the past because of interesting emission domains. Examples of such investigations can be found in reference papers such [10] for Cr^{3+}-doped garnets and Ti^{3+} doped oxides and [11] for Co^{2+} doped fluorides. Unfortunately, a restricted number of them have been lased, at low as well as at room temperature because of ESA.

The nature and the effect of charge transfer bands is more subtle. They would correspond to an electron charge delocalization (LMCT for Ligand to Metal Charge Transfer transition) from the surrounding (oxygen, fluorine, ...) ligands towards the active transition metal ions. They are usually very intense electric-dipole allowed optical transitions, 2 to 3 orders of magnitude stronger than the above considered vibronic transitions, and they generally occur in the near UV. Therefore, they do not perturb the emission processes. However, they seem to strongly influence the refractive index of the optically pumped materials and contribute to pseudo-nonlinear effects which still need to be clearly identified and eventually exploited. A good survey of that question has been made recently in the case of Cr^{3+} doped GSGG and Ruby (Cr^{3+} doped Al_2O_3) and can be found in Ref. [12].

The position of these LMCT absorption bands can be roughly determined by using the Jorgensen expression [13]:

$$E_{LMCT} \approx 30000\left[\chi_{opt}(L) - \chi_{unc}(M)\right] \tag{13}$$

where $\chi_{opt}(L)$ stands for the electronegativity of the ligands ($\chi_{opt}(O^{2-}) \approx 3.2$ and $\chi_{opt}(F^-) \approx 3.9$) and $\chi_{unc}(M)$ for the

electronegativity of the considered transition metal ions, uncorrected for spin correlation.

3. Laser crystals doped with active ions sitting in (near) octahedral environments

3.1. Ti^{3+} doped laser crystals

Nowadays, Ti:Sapphire (Ti^{3+}:Al$_2$O$_3$) is probably, with some other rare-earth doped materials, one of the most attractive laser crystals. Indeed, with its incredibly wide laser wavelength tunability (due to a very particular "Jahn-Teller" effect) extending from about 650 nm up to 1100 nm, its relatively large emission cross section (4.5 × 10^{-19} cm^2 in π polarization), its excellent thermo-mechanical properties and its availability in the form of large, uniformly doped and excellent optical quality single crystals [14–16], Ti:Sapphire now enters in a multitude of laser systems from standard medium high average power and broadly tunable continuous-wave (CW) lasers and ultra-short pulse laser oscillators to terawatt level amplifiers.

Nevertheless, the crystal growth of large (20 cm diameter) and uniformly doped single crystals with a high factor of merit (FOM), i.e. a ratio between absorption coefficients at the pump and laser wavelengths, of the order of a few hundreds, remain a challenge and a problem for the construction of the future high intensity laser chains. Additionally, very few companies are now able to provide such large size and high quality crystals.

Other problems encountered with Ti:Sapphire are its pump wavelength and emission lifetime. Indeed, Ti:Sapphire must be pumped around 500 nm (see in Fig. 1), but there is no high power semiconductor diodes, at present and certainly for a long time, available in this wavelength domain (which is often called the "Green-Gap" domain), and its emission lifetime (3.2 μs at room temperature) is too short to really store as much power as other systems based on Nd^{3+} or Yb^{3+}-doped laser materials. It is perfectly fine for laboratory purposes since many medium high power pump sources including CW and pulsed frequency-doubled Nd:YAG or Nd:YVO$_4$ solid-state lasers, or optically pumped semiconductor lasers (OPSL) can be used advantageously to pump the crystals around 500 nm. However, for the high intensity laser chains, CW OPSLs are useless and pulsed solid-state lasers become really complicated.

Several other materials with longer emission lifetimes or complementary absorption and emission domains such as Ti^{3+} doped

Fig. 1. Room temperature absorption/emission spectra of Ti:Sapphire (Al$_2$O$_3$) and Ti:Chrysoberyl (BeAl$_2$O$_4$) (see in Table 1 for calibration in cross section unit).

YAG [17], YAP [18,19], LMA [20,21], MgAl$_2$O$_4$ [22] and Chrysoberyl (BeAl$_2$O$_4$) [23–27] have been investigated in the past. Unfortunately, among all these materials, because of different problems related to crystal growth and the presence of impurity centers, excited-state absorption (ESA) and charge transfer bands, only Ti:Chrysoberyl has really led to laser action with significant laser performance. As a matter of fact, because of a slightly longer emission lifetime of 4.9 μs (stimulated emission cross section of about 4 × 10^{-19} cm^2) and a slightly shifted (towards the longer wavelengths) emission spectrum (see in Fig. 1) compared to Ti:Sapphire, Ti:Chrysobery is now reexamined in hybrid high power amplification laser chains combining both types of crystals to better control gain narrowing and gain saturation, which is quite interesting. However, although large size (1.5 cm diameter and 7 cm length) and good quality single crystals with FOM~100 have been already obtained, due to the complexity of the material, crystal growth of larger size and better quality crystals will certainly be very challenging. Moreover, Ti:Chrysoberyl (like Alexandrite Cr:BeAl$_2$O$_4$) is a biaxial orthorhombic system whose absorption and emission properties strongly depend on polarization along the direction of the three orthogonal crystallographic axes a, b and c. This will probably add to the complexity of the systems.

3.2. Laser materials based on V^{2+} and Cr^{3+} (3 d^{3+}), Ni^{2+} (3 d^8) and Co^{2+} (3 d^7) active ions

This category of laser materials can be subdivided further by considering those which led to room temperature CW and pulsed laser operation, i.e. Cr^{3+} doped oxides and fluorides, and those who only operated at cryogenic temperatures or at room temperature but by pumping them with flash-lamps or other pulsed lasers, i.e. V^{2+} (3 d^{3+}), Ni^{2+} (3 d^8) and Co^{2+} (3 d^7) doped fluorides, essentially. A summary of all these materials, their wavelength tuning range and their temperature of laser operation can be found in Ref. [28].

The first remark which can be made concerning these materials is that most of them were discovered and operated in the early days of tunable solid-state lasers, i.e. in the end of the seventies up to the end of the eighties, and that only few of them have really reached a commercial level.

Many Cr^{3+} doped oxides and fluorides have been lased successfully with rather good laser efficiencies at room temperature. They are characterized by broad absorption bands peaking around 450 nm and 600 nm (spin-allowed absorption transitions ^{4}A$_2$ → ^{4}T$_1$ and ^{4}A$_2$ → ^{4}T$_2$ with cross-sections of the order of 5 × 10^{-20} cm^2, depending on the materials — see in Fig. 2) which allow to pump them with flash-lamps, with standard frequency-doubled Nd:YAG or Nd:YVO$_4$ solid-state lasers, with OPSLs operating around 500 nm, or even in the red, with the aid of semiconductor diode lasers working around 650 nm, for medium and low-field crystalline materials like Cr:GSGG (Dq/B ≈ 2.45, B ≈ 638 cm^{-1} on the d^3 Tanabe Sugano T&S diagram) [29] and Cr:LiCAF (Dq/B ≈ 1.8, B ≈ 885 cm^{-1}) [30,31].

They are also characterized by emission lifetimes of a few tens of microseconds with provide good energy storage capabilities. Such relatively long emission lifetimes are resulting from the thermalization of the two metastable emitting levels ^{2}E and ^{4}T$_2$ (see T&S diagram for Cr^{3+} in Fig. 2) according to the expression given (in the absence of non-radiative relaxation) by:

$$\frac{1}{\tau_F} \approx \frac{(1/\tau_1) + (3/\tau_2)e^{-\Delta E/kT}}{1 + 3e^{-\Delta E/kT}} \tag{14}$$

where τ_1 is nearly equal to the emission lifetime associated with the ^{2}E → ^{4}A$_2$ spin-forbidden emission transition and τ_2 to the
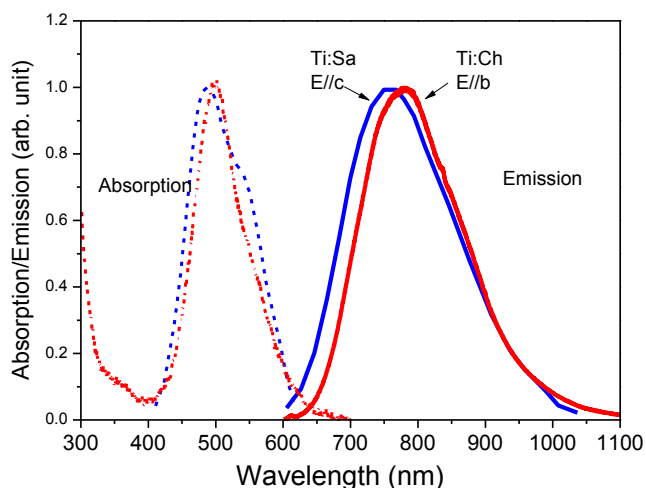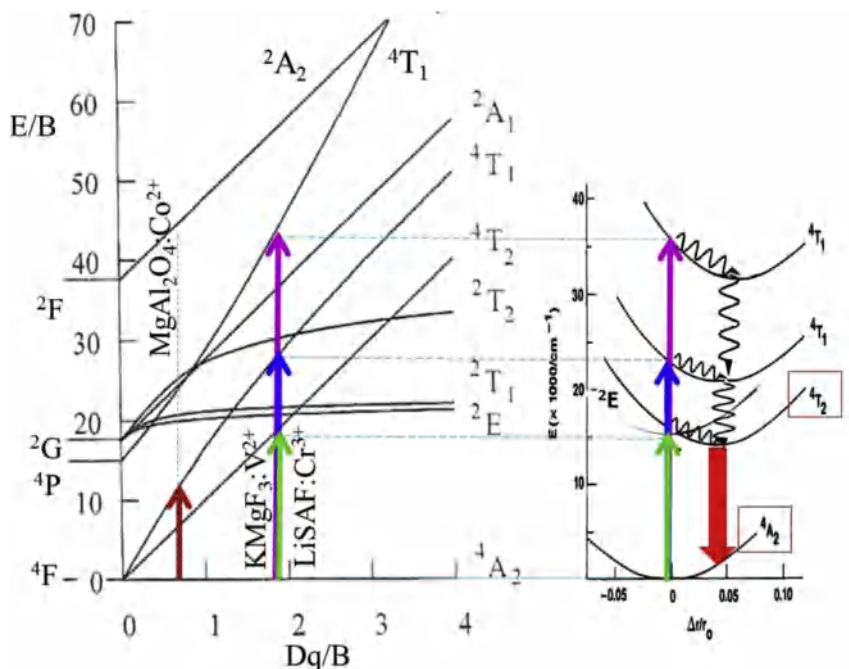
Fig. 2. Tanabe-Sugano and configuration curve diagrams along with optical transitions of the Cr^{3+} and V^{2+} ($Ar3d^3$) ions in nearly octahedral environments (LiSAF and KMgF$_3$, respectively) and of the Co^{2+} ($Ar3d^7$) ion in a nearly tetrahedral one (MgAl$_2$O$_4$).

emission lifetime associated with the $^4T_2 \rightarrow {}^4A_2$ spin-allowed one, depending on the relative positions of the ^2E and $^4T_2$ energy levels and their energy mismatch (energy difference between the deep parts of each configuration curve) $\Delta E = E(^4T_2) - E(^2E)$, thus depending on the nature of the host material and its Dq/B value. When ΔE is large and positive, like in the case of YAG ($\Delta E \approx 1500$ cm^{-1}), the measured emission lifetime is equal to a few milliseconds, whereas when ΔE is large and negative, like in the case of LLGG ($\Delta E \approx -900$ cm^{-1}), the measured lifetime is equal to a few tens of microseconds. In the same way, depending on the strength of the local crystal field experienced by the Cr^{3+} active ions, thus on the ΔE value, the vibronic emission spectra will be a combination of sharp $^2E \rightarrow {}^4A_2$ emission lines (the so-called R-lines) and of sharp zero-phonon and broad vibronic sidebands associated with a $^4T_2 \rightarrow {}^4A_2$ emission transition. For a medium-field laser material like Cr:GSGG, both types of emission transitions can be observed.

In the end, it is to be noticed that while most of these materials have been lased successfully, their effective laser tuning range is often substantially reduced compared to the one expected from their entire vibronic emission spectrum. Indeed, such broad-band emission spectra, with cross sections of about 10^{-20} cm^2, generally occur between about 650 and 1000 nm, but they strongly overlap, on their short wavelength side, with a strong $^4T_2 \rightarrow {}^4T_1(^4P)$ spin-allowed excited-state absorption (ESA) band peaking around 650 nm, and, on their long wavelength side, with another $^4T_2 \rightarrow {}^4T_1$ (^4F) spin-allowed ESA band peaking around 1100 nm. A laser system like Cr:GSGG, for instance, has been tuned between about 740 and 840 nm while its emission spectrum extends from 670 to 900 nm.

Consequently, in the last decades, only three laser systems (see in Fig. 3) have been really exploited for applications, and this for different reasons.

The first one is the Ruby laser, a flash-lamp pumped 3-levels laser system based on the high-field Cr:Al$_2$O$_3$ single crystal ($\Delta E \approx 2300$ cm^{-1}, $\tau_F \approx 3$ ms) and characterized by its sharp R-line laser emission at 694 nm, a system which is still used for some

paramedical applications. The second one is Alexandrite, or Cr:Chrysoberil, which is based on the medium/high-field Cr:BeAl$_2$O$_4$ laser crystal ($\Delta E \approx 800$ cm^{-1}, Dq/B ≈ 2.5, $\tau_F \approx 260$ µs), thus on a robust laser crystal like Ruby but which offers the possibility to be heated - up to about 150 °C, in which case $\tau_F \approx 70$ µs according to expr. (1) - to obtain a broad-band and tunable laser emission between about 700 and 820 nm. The third and, maybe, most important systems are the low-field colquiriites Cr:LiCAF ($\Delta E \approx -535$ cm^{-1}, $\tau_F \approx 160$ µs) and Cr:LiSAF ($\Delta E \approx -720$ cm^{-1}, $\tau_F \approx 65$ µs) [30] because of reduced non-radiative (multiphonon) relaxations, thus improved emission efficiencies, and the possibility to pump them with different kinds of laser sources including semiconductor diodes, as mentioned above. These two crystals have been used to build the most compact diode-pumped, tunable (720−840 nm) and ultra-short pulse
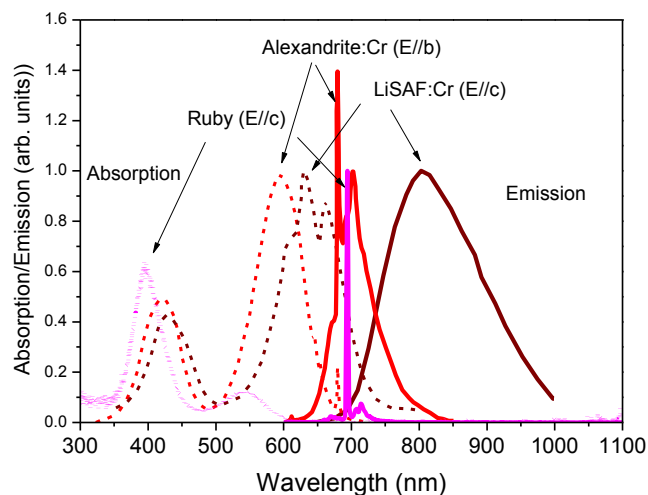
Fig. 3. Room temperature absorption (dashed curves) emission (solid curves) spectra of Ruby, Alexandrite and Cr:LiSAF (see in Table 1 for calibration in cross section unit).
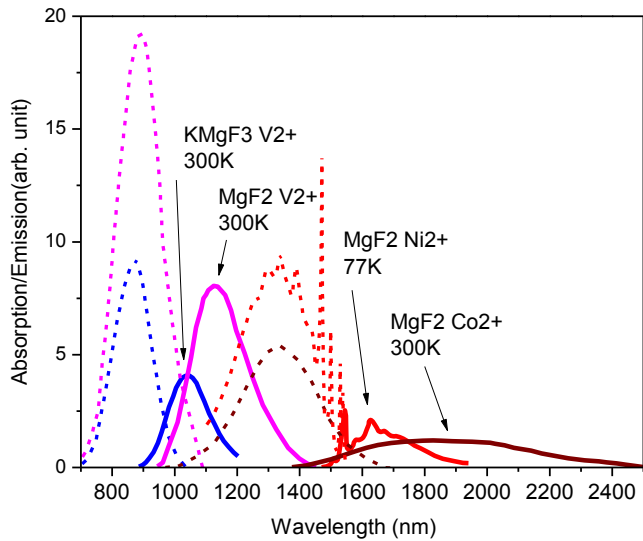
Fig. 4. Room temperature absorption (dashed curves) and emission (solid curves) spectra of V^{2+}, Ni^{2+} and Co^{2+} in the most important laser crystals (see in Table 1 for calibration in cross section unit).

(down to 10 fs) laser systems with the lowest laser thresholds even achieved [32–34]. They were also implemented as flash-lamp and diode pumped amplifiers in some high-power laser chains. The only problems reside in the robustness of the crystals and in their water durability which both need special cares [35,36].

A series of other very interesting laser systems based on V^{3+}(3 d^3), Ni^{2+} (3 d^8) and Co^{2+}(3d7) doped single crystals were also investigated in the past for their broad-band emission properties in the near- and mid-infrared regions. Except for Ni:MgO [37,38], most of them are fluorides, thus low-field systems, and were operated at cryogenic temperatures.

V^{2+} doped crystals [39] like MgF_2 and $KMgF_3$ [40] were investigated for their potential laser emissions between about 1 and 1.3 μm, thus beyond that offered by Ti^{3+} and Cr^{3+} doped materials. Unfortunately, both systems have been abandoned either because of strong non-radiative transitions and limited room temperature

emission efficiencies as well as reduced effective emission cross sections and restricted laser wavelength tuning range (because of a broad $^4T_2 \rightarrow {}^4T_1$ (^4F) spin-allowed ESA band) [41], which is the case of V:MgF₂, or simply because of limited absorption and emission cross sections of the order of 4×10^{-21} cm², which is the case of the cubic system V:KMgF₃. Nevertheless, V:KMgF₃ remains a very attractive system and could be worth to be reexamined by using more recent technological means. Indeed, it could work at room temperature with a fluorescence emission lifetime $\tau_F \approx 1.05$ ms (for a radiative one $\tau_R \approx 1.2$ ms), which means a large energy storage capability and a high fluorescence quantum efficiency $\eta \geq 85\%$. It could be efficiently pumped, like Yb^{3+} ions, with high power laser diodes working around 940 or 980 nm, thanks to negligible spin-forbidden $^4T_2 \rightarrow {}^2A_1, {}^2T_1, {}^2T_2$ ESA transitions (see in Fig. 2 the T&S diagram for 3 d^3 ions with Dq ≈ 1091 cm^{-1} and B ≈ 616 cm^{-1}, thus Dq/B ≈ 1.8 [41]). Its laser wavelength could be tuned between about 0.95 and 1.15 μm thanks to a negligibly small spin-allowed $^4T_2 \rightarrow {}^4T_1$ (^4F) ESA transition in the considered emission domain [41] thus with a quite low quantum "defect" (quantum shift between the pump and laser emission wavelengths λ_P and λ_L given by $\tau_{QD} \approx 1 - \frac{\lambda_P}{\lambda_L} \approx 7\%$.

Concerning Ni^{2+} (3 d^8 ion) doped materials, as mentioned above, except for Ni:MgO which was interesting because it was the only (high-field) crystal which could be operated at room temperature and around 1.3–1.4 μm [37,38] but which was abandoned because of an extraordinary difficult high-temperature crystal growth, all the other systems were fluorides and only worked at cryogenic temperatures around 77 K [28]. Among them, Ni:MgF₂ is probably the most important one as it could be lased, in spite of a strong $^3T_2 \rightarrow {}^3T_1$ (^4F) spin-allowed ESA transition (see in Fig. 5 the T&S diagram for the 3 d^8 ions with Dq ≈ 665 cm^{-1}, B ≈ 1000 cm^{-1}, thus Dq/B ≈ 0.67, and in Ref. [42]) between about 1.61 and 1.74 μm [43] (for a total emission range going from 1.5 up to 1.95 μm), and by pumping with a conventional CW Nd:YAG laser operating at 1.32 μm (transition $^3A_2 \rightarrow {}^3T_2$). Following the spectroscopic results reported in Refs. [42,44] and the laser results obtained by pumping the system with a Krypton laser at 752.5 nm (transition $^3A_2 \rightarrow {}^3T_1$ (^4F)) [45], two kinds of laser experiments could be carried out in the future with this interesting laser material. Its near-infrared laser properties could be reexamined by pumping with laser diodes
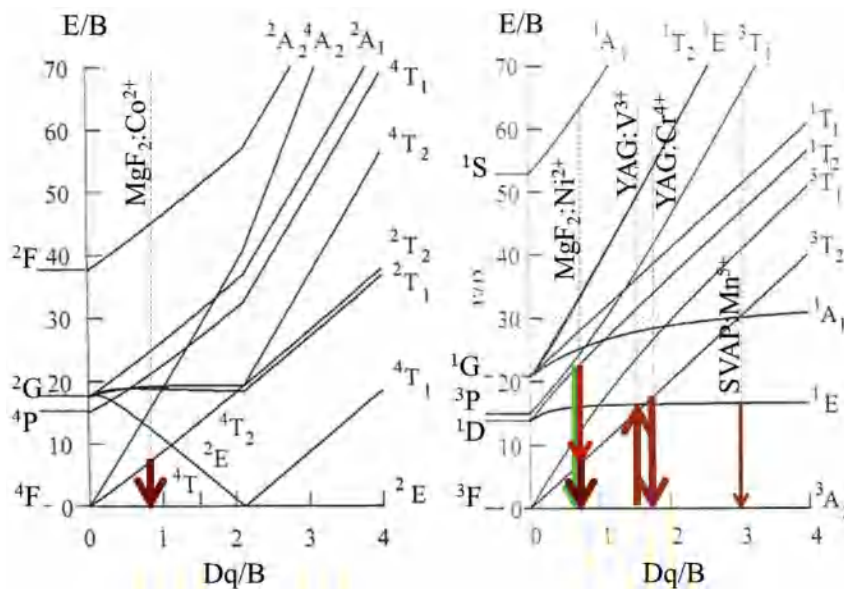
Fig. 5. Tanabe-Sugano diagrams along with emission transitions of Co^{2+} (Ar3d^7 ion) in MgF_2 (nearly octahedral symmetry), on the left, of Ni^{2+} (Ar3d^8 ion) in MgF_2, and of V^{3+}, Cr^{4+} and Mn^{5+} (Ar3d^2 ions) in the near tetrahedral environments of YAG and SVAP, on the right.

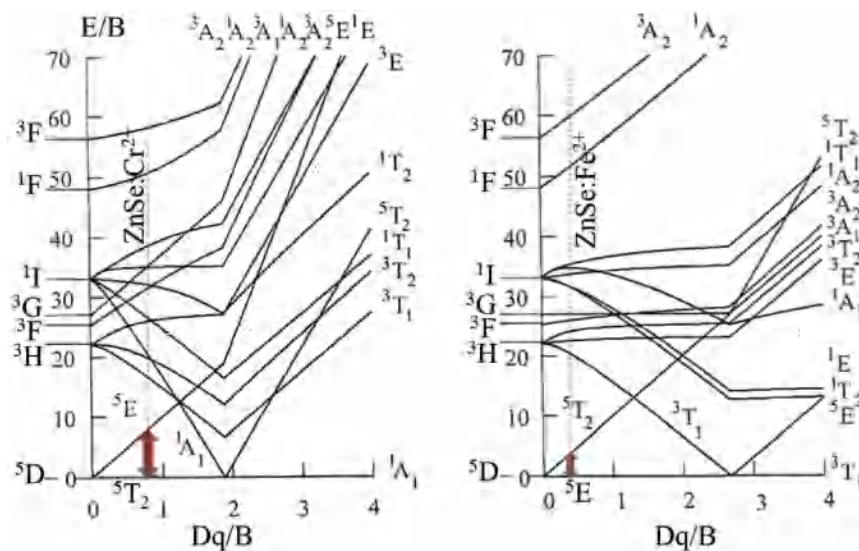**Fig. 6.** Tanabe-Sugano diagrams for tetrahedrally coordinated Cr^{2+} (3 d^4, T&S diagram for 3 d^6), on the left, and Fe^{2+} (3 d^6, T&S diagram for 3 d^4) ions, on the right.

around 800 nm, in a wavelength range where no ESA should occur, and the laser potential of its green and red emissions ($^1T_2 \rightarrow {}^3A_2$ and $^1T_2 \rightarrow {}^3T_2$) could be worth to be investigated more specifically once pump laser diodes will be available around 420 nm ($^3A_2 \rightarrow {}^3T_1$ (^4P) absorption transition).

Last in the series are the Co^{2+} (Ar3d^7 ion) doped crystals with essentially two types of fluoride systems whose detailed ground- and excited-state spectroscopy were reported in Refs. [46–49]: the low-field orthorhombic crystal Co:MgF$_2$ (associated — see in Fig. 5 — with a Dq/B value of about 0.84) and the isotype cubic crystals Co:KMgF$_3$ and Co:KZnF$_3$ (associated with a Dq/B value of about 0.86). In fact, only the first one has reached a commercial level for a while [50], in particular for atmospheric remote sensing and intracavity laser spectroscopy of different molecules [51,52]. It could be lased quite efficiently and tuned in a very wide spectral range, between about 1.51 and 2.4 μm, in the CW regime and at liquid nitrogen temperature, by pumping with a CW Nd:YAG laser operating at 1.32 μm [53]. Co:MgF$_2$ was also operated at room temperature in the QCW regime, but in a more restricted spectral range (1.75–2.5 μm) [48–50,54] by pumping again at 1.32 μm but with a free-running Nd:YAG laser delivering pulses of a few tens of microseconds. It is worth noting here that Co:MgF$_2$ could be operated at room temperature in spite of a very reduced fluorescence quantum efficiency. Indeed, due to the large electron-phonon coupling and the number of allowed promoting phonon modes which can induce non-radiative multiphonon relaxations between the $^4T_2$ and the $^4T_1$ (^4F) emitting- and ground states of Co^{2+} in this orthorhombic crystal (see in Fig. 4 the T&S diagram for 3 d^7 ion), its emission lifetime is decreasing from about 1.6 ms at T = 12 K down to about 40 μs at T ≈ 300 K, thus resulting in a fluorescence quantum efficiency of about 2.5%.

4. Laser crystals and saturable absorbers based on active ions sitting in (near) tetrahedral environments

A lot was known about the spectroscopy of these materials already in the beginning of the sixties, with important reports Pappalardo, Weakliem et al. [55,56] for Ni^{2+} and Co^{2+} in chlorides, bromides, sulfides and oxides, from Ferguson, Wood et al. [57,58] for Co^{2+} in aluminum and gallium oxides, from Baranowski et al. [59] for Co^{2+} in sulfides, selenides, tellurides, phosphides and arsenides, from McClure, Tanabe and Sugano [60,61] for V^{3+} in

oxides, from Avinor, Meijer and Allen [62,63] for V^{3+} in sulfides and selenides, from Slack et al. [64,65] for Fe^{2+} (3 d^6) in oxides, sulfides and tellurides, and from Baranowski, Vallin, Nelkowski e al [59,65–67] for Fe^{2+} in selenides, tellurides, sulfides, phosphides and arsenides.

4.1. Principal laser systems

Their interest as laser materials really starts at the end of the eighties, beginning of the nineties, first with the Cr^{4+} (3 d^2) doped oxides Cr:Mg$_2$SiO$_4$ (Forsterite) and Cr:YAG (also called "black garnet"), with the laser demonstrations reported in Refs. [68] and [69] respectively, then with the Cr^{2+} (3 d^4 ion) doped selenide Cr:ZnSe and the pioneer's works reported in Refs. [70–72] with the laser properties of Cr^{2+} then of Fe^{2+} in ZnSe [73–75].

Concerning the former, it is worth noting here that almost no data was available at that time on the spectroscopy of the Cr^{4+} ion in a tetrahedral symmetry site. Moreover, since Cr^{3+} and Cr^{4+} ions could coexist in systems like Mg$_2$SiO$_4$ and YAG, it was easy to

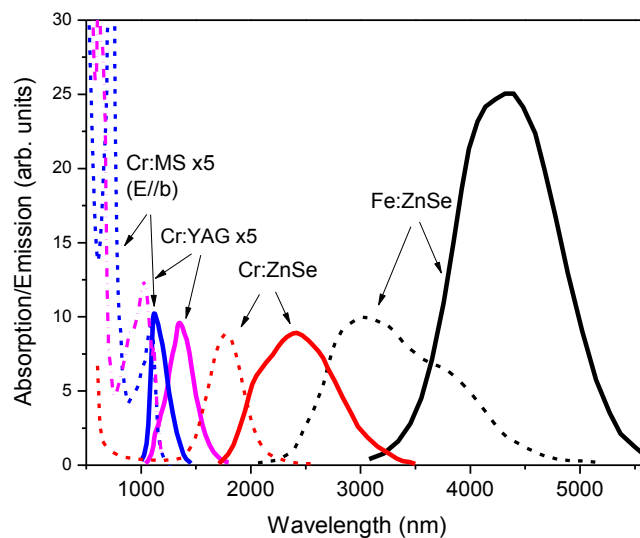**Fig. 7.** Room temperature absorption (dashed curves) and emission (solid lines) spectra of Cr^{4+} (3 d^2), Cr^{2+} (3 d^4), Co^{2+} (3 d^7) and Fe^{2+} (3 d^6) ions sitting in (near) tetrahedral environments (see in Table 1 for calibration in cross section unit).

misinterpret the absorption and emission spectra. This is the reason why Petricevic et al. first wrongly assigned the lasing emission observed around 1.23 µm in Cr:Forsterite to Cr^{3+} ions in a low crystal field environment, and Angert et al. [69] the laser emission observed around 1.4 µm in Cr:YAG to some impurity color center associated with the oxidation of the chromium dopants to the quadrivalent state. It was quickly recognized, however, in the case of Cr:Forsterite [76–78] then of Cr:YAG [79–81], that the positions of the optical transitions, their high cross-sections (of the order of 10^{-19}–10^{-18} cm²) and their short emission lifetimes (3 µs for Cr:Forsterite and 4.1 µs for Cr:YAG) could not be assigned to octa-hedrally coordinated Cr^{3+} ions but to Cr^{4+} ions in lattice sites of tetrahedral symmetry (the Si^{4+} lattice sites in the case of Cr:Forsterite, for instance [82].

As indicated in Section 2a the energy levels for 3dⁿ ions in (near) tetrahedral crystalline environments are given by the T&S diagrams for the 3 d^{10-n} ions with complementary electronic configurations in (near) octahedral crystal fields. Therefore, for instance, the energy levels of the tetrahedrally coordinated Cr^{4+} (3 d²) and Cr^{2+} (3 d⁴) ions are giving by the T&S diagrams for the 3d⁸ (see in Fig. 5) and 3d⁶ ions (see in Fig. 6).

Consequently, in the case of Cr:Forsterite, the sequence of ground- and excited-states is the same as for octahedrally coordinated Ni^{2+} ions, i.e. ³A₂, ³T₂, ³T₁(³F), ³T₁(³P), and the observed laser emission is assigned to a ³T₂ → ³A₂ spin-allowed transition. More precisely, the SiO₄ tetrahedra in which the Cr^{4+} ions substitute in this material having a symmetry close to a C₃ᵥ trigonal symmetry (instead of pure T_d tetrahedral one) with the three-fold symmetry axis parallel to the a axis of the crystal, each above mentioned crystal-field spectral term splits into lower symmetry ones, such as ³A₂ and ²E for the first excited state ³T₂. Making the approximation of a pure T_d tetrahedral site symmetry (what is not correct), a rough description of the entire sequence of energy levels for Cr:Forsterite is obtained with the T&S diagram for a 3 d⁸ ion (see in Fig. 4) with a Dq/B value of about 1 and B ≈ 900 cm⁻¹ [76,83].

In the case of the Cr:YAG black garnet [83–85] it was demonstrated that the Cr^{4+} ions were sitting in a nearly-tetrahedral environment (S₄ symmetry) corresponding to a large ligand field with Dq/B = 1.8 (much larger than in the case of Cr:Forsterite). Therefore, according to the T&S energy level diagram for d⁸ ions, the lowest metastable excited state is a ¹E singlet and the broad band emission (1.1–1.6 µm) which is observed at room temperature in this material (see in Fig. 7) with an emission lifetime of 4.1 µs is actually due to a thermal admixture of ¹E and ³T₂ emitting levels [86,87].

Many other Cr-doped crystals with tetrahedrally coordinated Cr^{4+} ions, including a series of mixed garnets [88], silicates [89–93] (for the most important ones), and some germanates [94–97] were investigated afterwards because of complementary emission domains. However, only Cr:Forsterite and Cr:YAG (see in Fig. 7) have reached a certain level of maturity and have been really exploited. Both have been lased in the CW and the mode-locked (ML) regimes with laser tuning ranges extending from about 1170 to 1370 nm in the case of Cr:Forsterite [98] and from 1309 to 1596 nm in the case of Cr:YAG [99,100] and laser pulses as short as 20 fs at 1300 nm in the case of Cr:Forsterite [101,102] and 53 fs at 1540 nm in the case of Cr:YAG [103].

Several crystals (fluorovanates) were also investigated with pentavalent Mn^{5+} ions in tetrahedral environments [90]. As they are 3 d² ions, like Cr^{4+}, their spectroscopy is described by the same T&S diagram as for 3 d⁸ ions. However, they are associated with a crystal field even larger than in the case of Cr^{4+}:YAG with Dq/B ≈ 3. In this case, at room temperature, there is no thermalization between the ¹E and ³T₂ emitting states and the only possible emission is a ¹E → ³A₂ spin-forbidden optical transition having the form of a

sharp line (like in the case of ruby for crystals doped with Cr^{3+} ions) and a long emission lifetime of the order of 1 ms [90,104]. None of these crystals have really lased efficiently and they have been quickly abandoned.

In the case of Cr^{2+}:ZnSe, as given by the T&S energy level diagram for octahedrally coordinated 3 d⁶ ions (see in Fig. 6) with a Dq/B value of about 0.8 [105], the ground-state for the tetrahedrally coordinated Cr^{2+} (3 d⁴) ions is a ⁵T₂ crystal field spectral term and the first excited ones ⁵E, ³T₁, ³T₂, etc. . Therefore, the first absorption band peaking around 1.8 µm and the broad emission one extending from 1.6 to 3.2 µm in this material (see in Fig. 7) are associated with ⁵T₂↔⁵E spin-allowed optical transitions. As indicated by the diagram, it is clear that no (negligible) ESA is expected and was detected neither at the pump nor at the laser wavelengths [106] since the only possible ESA absorption transitions originating from the ⁵E metastable emitting state are spin-forbidden transitions. This constitutes one of the major advantages of this very efficient laser system. With absorption and emission cross sections of the order of 10^{-19} cm², a room temperature emission lifetime of about 8.7 µs and a corresponding emission quantum efficiency close to 1, Cr:ZnSe is now considered as one of the major solid-state laser materials and it is sometimes called the "Ti:Sapphire laser of the mid-infrared". It has been lased in the CW and ML regimes (with the production of ultra-short laser pulses down to 69 fs [107] by pumping with different kinds of laser sources including Er^{3+} doped fibers operating around 1.58 µm, solid-state lasers based on Tm^{3+}doped single crystals such as Tm:YAP or Tm:YAG operating around 1.95 µm and InGaAsP semiconductor laser diodes working around 1.55 µm. Its laser wavelength could be tuned between 2 and 3.1 µm, which is a record never reached by any other ion-doped solid-state laser material.

The situation found in the case of Fe^{2+} doped chalcogenides such as Fe^{2+}:ZnSe and Fe^{2+}:ZnS is very similar to that found with Cr^{2+}. Fe^{2+} is a 3 d⁶ ion. Therefore, in a tetrahedral environment, its energy levels are those found with the T&S diagram for d⁴ ions in octahedral symmetry (see in Fig. 6). The only spin-allowed optical transitions are the absorption and emission transitions occurring between the ⁵E and ⁵T₂ energy levels. No significant ESA transition occurs at the pump and the emission wavelengths. Compared to Cr^{2+}, the splitting of the ⁵D spectral term which gives to the ⁵E and ⁵T₂ energy levels is just reversed. This is what is expected for ions having complementary electronic configurations, here 3 d⁶ and
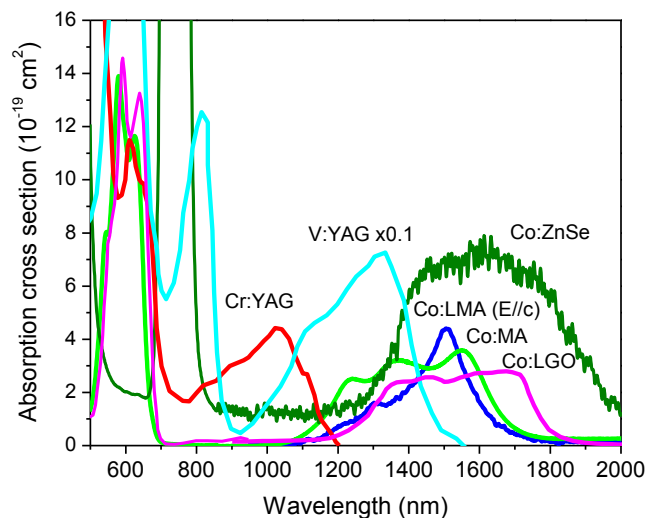

Fig. 8. Room temperature absorption spectra of V^{3+}, Cr^{4+} (3 d²) and Co^{2+} (3 d⁷) doped crystals - ions sitting in (near) tetrahedral environments - used as saturable absorbers.

Table 1
Spectroscopic characteristics of main laser materials.

Material	Type of material: Laser/SA	Main absorption wavelength, cross section and polarization	Main emission wavelength, cross section and polarization	Emission and radiative lifetimes	Typical dopant concentration
Ti^{3+}:Al_2O_3 (Ti:Sapphire)	Laser	485 nm 9.3×10^{-20} cm^2 E//c	760 nm 4×10^{-19} cm^2 E//c	3.15 µs 3.85 µs	0.1 wt%Ti_2O_3 3.3×10^{19} cm^{-3}
Ti^{3+}:$BeAl_2O_4$ (Ti:Chrysoberil)	Laser	500 nm 1.3×10^{-20} cm^2 E//b	780 nm 2×10^{-19} cm^2 E//b	5 µs 6.4 µs	3×10^{19} cm^{-3}
Cr^{3+}:Al_2O_3 (Ruby)	Laser	550 nm 2.2×10^{-19} cm^2 E⊥c	694 nm 3×10^{-20} cm^2	2.9 ms	1.9×10^{19} cm^{-3}
Cr^{3+}:$BeAl_2O_4$ (Alexandrite)	Laser	590 nm 2.6×10^{-19} cm^2 E//b	740 nm 3×10^{-20} cm^2 at 200 °C E//b	260 µs (28 °C) 76 µs (150 °C)	0.05 at% 2.05×10^{19} cm^{-3} (75% of the ions in C$_s$ laser active sites)
Cr^{3+}:$LiSrAlF_6$ (Cr:LiSAF)	Laser	638 nm 5.5×10^{-20} cm^2 E//c	846 nm 4.8×10^{-20} cm^2 E//c	67 µs	1.7 at% 1.4×10^{20} cm^{-3}
V^{2+}:MgF_2	Laser	890 nm 1.9×10^{-20} cm^2	1130 nm 0.8×10^{-20} cm^2	≤20 µs 2.3 ms	1 at% 3×10^{20} cm^{-3}
V^{2+}:$KMgF_3$	Laser	870 nm 0.9×10^{-20} cm^2	1040 nm 4×10^{-21} cm^2	1.05 ms 1.2 ms	0.5 at% 7.8×10^{19} cm^{-3}
Ni^{2+}:MgF_2	Laser	1370 nm 8.8×10^{-21} cm^2 E//c	1620 nm 2.1×10^{-21} cm^2 E//c	3 ms 11.5 ms	1 at% 3×10^{20} cm^{-3}
Co^{2+}:MgF_2	Laser	1350 nm 5.3×10^{-21} cm^2 E//c	2050 nm 1.2×10^{-21} cm^2 E//c	40 µs 1.4 ms	1 at% 3×10^{20} cm^{-3}
Cr^{4+}:Mg_2SiO_4 (Cr:Forsterite or Cr:MS)	Laser	1064 nm 1.7×10^{-19} cm^2 E//b	1120 nm 2×10^{-19} cm^2 E//b	3.6 µs	0.13mol% 1.8×10^{19} cm^{-3}
Cr^{4+}:$Y_3Al_5O_{12}$ (Cr:YAG)	Laser and SA	1064 nm 2.2×10^{-19} cm^2	1440 nm 1.9×10^{-19} cm^2	4.2 µs	5.5×10^{-18} cm^{-3}
V^{3+}:YAl_5O_{12} (V:YAG)	SA	1342 nm 7.2×10^{-18} cm^2	—	22 ns	2×10^{20} cm^{-3} (less than 1% in tetrahedral sites)
Co^{2+}:$MgAl_2O_4$ (spinel)	SA	1.54 µm 3.5×10^{-19} cm^2	—	350 ns	5.5×10^{18} cm^{-3}
Co^{2+}:$LaMgAl_{11}O_{19}$ (Co:LMA)	SA	1.54 µm 4.4×10^{-19} cm^2 E//c	—	210 ns	10^{19} cm^{-3}
Co:$LiGa_5O_8$ (Co:LGO)	SA	1.54 µm 2.5×10^{-19} cm^2	—	130 ns	3.3×10^{-19} cm^3
Co^{2+}:ZnSe	SA	1625 nm 7.4×10^{-19} cm^2	3300 nm 3.6×10^{-20} cm^2	290 µs	$3–4 \times 10^{18}$ cm^{-3}
Cr^{2+}:ZnSe	Laser and SA	1760 nm 8.8×10^{-19} cm^2	2400 nm 8.9×10^{-19} cm^2	7.8 µs	1.5×10^{19} cm^{-3}
Fe^{2+}:ZnSe	Laser	3000 nm 10^{-18} cm^2	4400 nm 2.5×10^{-18} cm^2	370 ns	$1–3 \times 10^{18}$ cm^{-3}

3 d^4, the maximum number of electrons for a d shell being equal to 10.

A system like Fe^{2+}:ZnSe which is associated with Dq/B and B values of about 0.35 and 1000 cm^{-1}, respectively, is thus characterized by strong absorption and emission transitions having the form of broad bands peaking around 3–3.5 µm and 4–4.5 µm with cross sections of about 1×10^{-18} and 2.5×10^{-18} cm^2 (see in Fig. 7). Its low temperature emission lifetime is of the order of 100 µs but it decreases down to about 370 ns at room temperature. Consequently, such as laser system perfectly works at cryogenic temperatures (say below about 200 K) but is more difficult to operate at room temperature.

4.2. Principal saturable absorbers

The interest of tetrahedrally coordinated transition metal ions as saturable absorbers for passive Q-switching of various solid-state laser sources has really appeared at about the same time (end of the eighties) as some of them, like Cr:YAG [108] were studied for their broad-band laser properties. Three types of materials have been really exploited: Cr^{4+}:YAG, Cr^{4+}:LuAG [109] and Cr^{4+}doped silicates [110,111] for intracavity Q-switching of 1.06 µm Nd-based lasers, V^{3+}:YAG for Q-switching of 1.32 µm lasers [112], Co^{2+} doped magnesium spinels Co^{2+}:MgAl$_2$O$_4$ (MA) [113] and Co^{2+}:LaMgAl$_{11}$O$_{19}$ (LMA) [114] as well as Co^{2+}:LiGa$_5$O$_8$ (**LGO**) [115] for Q-switching of 1.32 µm and 1.54 µm lasers, and also Co^{2+} and Cr^{2+} doped chalcogenides like ZnSe, ZnS and CdMnTe for Q-switching of 1.54 µm and 2 µm eye-safe lasers [116–119].

In the case of crystals doped with Cr^{4+} ions, it is the absorption band (see in the T&S diagram for 3 d^8 ions and in Fig. 8) corresponding to the first spin-allowed absorption transition $^3A_2 \rightarrow {}^3T_2$ peaking around 1 µm (Dq/B ≈ 1.8) which saturates at high intracavity circulating powers in 1.06 µm Nd-based lasers [111].

In the case of V^{3+}(3 d^2 ion like Cr^{4+} and T&S diagram for 3 d^8), it is again the same $^3A_2 \rightarrow {}^3T_2$ spin-allowed absorption band which is involved but around 1.32 µm (see in Fig. 8) due to a lower crystal field (Dq/B ≈ 1.5 and B ≈ 535 cm^{-1}) [112].

In the case of Co^{2+} (3 d^7 ion and T&S diagram for d^3), the absorption spectra consist of three broad bands: a very weak one corresponding to the low energy absorption transition $^4A_2 \rightarrow {}^4T_2$,

and two strong ones associated with the spin-allowed and higher energy absorption transitions $^4A_2 \rightarrow {}^4T_1(^4F)$ and $^4A_2 \rightarrow {}^4T_1(^4P)$. For spinels, these broad absorption bands are peaking around 2750 nm, 1600 nm and 600 nm (see in Fig. 8). On the T&S diagram, they correspond to a crystal field parameter Dq/B ≈ 0.65 with B ≈ 545 cm^{-1}. The lifetime of the emission coming from the $^4T_2$ metastable level is very short, with a value of about 200 ns in the case of Co^{2+}:LMA for instance [114]. Such crystals are used in fact as passive Q-switchers for lasers operating around the peak of the second absorption band and more particularly for Er-based eye-safe lasers emitting around 1.54 μm [113,118,119]. They can be used as well for passive Q-switching of other mid-infrared lasers operating at longer wavelengths, such as Tm-based lasers emitting around 1.9 μm [117].

The first broad absorption band peaking around 1.8 μm mentioned above in the case of the tetrahedrally coordinated Cr^{2+} doped chalcogenides like ZnSe ($^5T_2 \rightarrow {}^5E$ spin-allowed optical transition) can be also used for passive Q-switching Tm- and Ho-based solid state lasers operating around 2 μm [120]. In that case, saturation occurs in spite of a ^2E metastable level with an emission lifetime of several μs: 8 μs in the cases of Cr^{2+}:ZnSe and Cr^{2+}:ZnS at room temperature, for example [70].

5. Summary and conclusion

The spectroscopic characteristics of the main laser materials (laser emitting materials as well as saturable absorbers) based on transition metal ions which can be operated at room temperature have been reviewed. As discussed in the Section 2 then developed in the Section 3 and synthetized in Table 1 where we have gathered the cross sections at the main absorption and emission wavelengths used to operate these materials as well as their characteristic emission lifetimes, these laser materials can be divided into two categories. The first category consists of crystals doped with Ti^{3+}, Cr^{3+}, V^{2+}, Ni^{2+} and Co^{2+} occupying sites of (near) octahedral symmetry. They are characterized by broad bands with cross sections ranging between 10^{-21} to 10^{-19} cm^2 and emission lifetimes between a few tens of μs to several ms. They are essentially used as laser emitting materials in the near- and the mid-infrared, either for their wide wavelength laser tunability and/or the production of ultra-short laser pulses. The second category consists of crystals doped with V^{3+}, Cr^{4+}, Co^{2+}, Cr^{2+} and Fe^{2+} occupying sites of (near) tetrahedral symmetry. They are also characterized by very broad bands but with much higher absorption and emission cross sections (several 10^{-19} up to several 10^{-18} cm^2) and shorter emission lifetimes (few μs down to few hundreds of ns) because of strong spin- and parity-allowed optical transitions. Among these materials, only those doped with Cr^{4+}, Cr^{2+} and Fe^{2+} have been efficiently operated as laser emitting materials, either, as the previous ones, for their wide laser wavelength tunability or the production of ultra-short laser pulses. All the other materials, those doped with V^{3+} and Co^{2+} ions, as well as some materials doped with Cr^{4+} or Cr^{2+} ions, have been essentially used as saturable absorbers for other mid-infrared solid state lasers operating around 1.32 μm, 1.54 μm and 2 μm.

In conclusion, the laser materials based on transition metal ions, because of their unique properties, are still been used and exploited for various kinds of applications. Most of them, however, have been operated as bulk crystals and pumped with other more or less complicated solid-state laser sources. Although some attempts have been already made in the past in that direction, very interesting results should be expected in the future by revisiting and operating these materials in the form of waveguides, to decrease the laser thresholds and increase the laser efficiencies, and by pumping them with the laser diodes which are presently developed from the blue to the mid-infrared.

References

[1] Y. Tanabe, S. Sugano, J. Phys. Soc. Jpn. 9 (1954) 753–779.
[2] M.G. Brik, A.M. Srivastava, Opt. Mater. 35 (2013) 1776–1782.
[3] B. Henderson, G.F. Imbush, Optical Spectroscopy of Inorganic Solids, Oxford University Press, 2006.
[4] J.S. Griffith, Theory of Transition Metal Ions, Cambridge University Press, 1964.
[5] B. Henderson, R.H. Bartram, Crystal-field Engineering of Solid-state Laser Materials, Cambridge University Press, 2005, p. 108.
[6] W.H. Fonger, C.W. Struck, Phys. Rev. B 11 (1975) 3251.
[7] F. Auzel, in: B. Di Bartolo (Ed.), Radiationless Processes, Plenum Press, N.Y, 1980.
[8] R.H. Bartram, J.C. Charpie, L.J. Andrews, A. Lempicki, Phys. Rev. B 34 (1986) 2741.
[9] S.A. Payne, L.L. Chase, G.D. Wilke, J. Lumin. 44 (1989) 167.
[10] K. Petermann, Opt. Quant. Electron. 22 (1990) S199–S218.
[11] H. Manaa, R. Moncorgé, Opt. Quant. Electron. 22 (1990) S219–S226.
[12] Th. Godin, R. Moncorgé, J.L. Doualan, M. Fromager, K. Ait-Ameur, R.A. Cruz, T. Catunda, J. Opt. Soc. B 29 (5) (2012) 1055.
[13] C.K. Jorgensen, Mol. Phys. 5 (1962) 271.
[14] D. Joyce, B. Ripley, K. Schmid and S. Cohen, Laser Focus World, 03/01/2010 Issue.
[15] A. Nehari, A. Brenier, G. Panzer, K. Lebbou, J. Godfroy, S. Labor, H. Legal, G. Cheriaux, J. Chambaret, T. Duffar, R. Moncorgé, Cryst. Growth Des. 11 (2) (2011) 445–448.
[16] R. Moncorgé, J.L. Doualan, IEEE J. Sel. Top. Quant. Electron. 21 (1) (2015) 2357995.
[17] F. Bantien, P. Albers, G. Huber, J. Lumin. 36 (1987) 363.
[18] J. Kvapil, M. Koselja, J. Kvapil, B. Perner, V. Skoda, J. Kubelka, K. Hamel, V. Kubecek, Czech. J. Phys. B 38 (1988) 237.
[19] K. Petermann, Opt. Quant. Electron. 22 (1990) S199–S218.
[20] C. Wyon, J.J. Aubert, D. Vivien, A.M. Lejus, R. Moncorgé, J. Lumin. 40/41 (1988) 871.
[21] D. Gourier, L. Colle, A.M. Lejus, D. Vivien, R. Moncorgé, J. Appl. Phys. 63 (4) (1988) 1144.
[22] W. Strek, P. Deren, B. Jerowska-Trzebiatowska, J. Phys. Paris. C7 48 (Suppl. 12) (1987) 455.
[23] A.I. Alimpiev, G.V. Bukin, V.N. Matrosov, E.V. Pestryakov, V.P. Solntsev, V.I. Trunov, E.G. Tsvetkov, V.P. Chebotaev, Sov. J. Quant. Electron. 16 (1986) 579.
[24] E.V. Pestryakov, V.I. Trunov, A.I. Alimpiev, Sov. J. Quant. Electron. 17 (1987) 585.
[25] A. Sugimoto, Y. Segawa, P.H. Kim, S. Namba, K. Yamagishi, Y. Anzai, Y. Yamaguchi, J. Opt. Soc. Am. B16 (1989) 2334.
[26] N. Sarukura, Y. Segawa, K. Yamagishi, in: A.A. Pinto, T.Y. Fan (Eds.), OSA Proc. ASSL 1993, vol. 15, 1993, p. 299.
[27] H. Cao, X. Lu, D. Fan, Appl. Opt. 51 (12) (2012) 2150.
[28] R. Moncorgé, SPIE Vol. 1182, French-israeli Workshop on Solid-state Lasers, 1988, pp. 34–48.
[29] B. Struve, G. Huber, Appl. Phys. B36 (1985) 195.
[30] S.A. Payne, L.L. Chase, G.D. Wilke, J. Lumin. 44 (1989) 167.
[31] K.P. O'Donnell, A. Marshall, M. Yamaga, B. Henderson, B. Cockaine, J. Lumin. 42 (1989) 365–373.
[32] Ph. Wagenblast, R. Ell, U. Morgner, F. Grawert, F.X. Kartner, Opt. Lett. 28 (18) (2003) 1713.
[33] G.J. Valentine, J.M. Hopkins, P. Loza-Alvarez, G.T. Kennedy, W. Sibbett, Opt. Lett. 22 (21) (1997) 1639.
[34] D. Kopf, K.J. Weingarten, G. Zhang, M. Moser, M.A. Emanuel, R.J. Beach, J.A. Skidmore, U. Keller, Appl. Phys. B 65 (1997) 235–243.
[35] S.A. Payne, L.K. Smith, R.J. Beach, B.H.T. Chai, J.H. Tassano, L.D. DeLoach, W.L. Kway, R.W. Solarz, W.F. Krupke, Appl. Opt. 33 (24) (1994) 5526.
[36] B. W Woods, S.A. Payne, J.E. Marion, R.S. Hughes, L.E. Davis, J. Opt. Soc. Am. B8 (5) (1991) 970.
[37] A. Mooradian, Laser Focus 15 (1979) 28.
[38] P.F. Moulton, in: M.J. Weber (Ed.), Handbook of Laser Science and Technology I, Lasers and Masers, Chemical Rubber Company, Boca Raton, 1982, pp. 50–60.
[39] W. Knierim, A. Honold, V. Brauch, V. Durr, J. Opt. Soc. Am. 3 (1986) 119–124.
[40] P.F. Moulton, Workshop on tunable solid state lasers, Fort Belvoir, Virginia, in: J.C. Walling (Ed.), in: A. B.Budgor, L. Esterowitz, L.G. Deshazer (Eds.), Proc. Of the Tunable Laser Conference II Zigzag, Oregon, Vol. 52, Springer-Verlag, Berlin, 1983–1986, p. 196.
[41] R. Moncorgé, T. Benyattou, Phys. Rev. B 37 (16) (1988) 9177.
[42] R. Moncorgé, T. Benyattou, Phys. Rev. B 37 (16) (1988) 9186.
[43] P.F. Moulton, A. Mooradian, Appl. Phys. Lett. 35 (1979) 838.
[44] R. Moncorgé, F. Auzel, J.M. Breteau, Phil. Mag. B 51 (1985) 489.
[45] F. Auzel, R. Moncorgé, J. Opt. Paris. 15 (5) (1984) 338–435.
[46] W. Kunzel, W. Knierim, U. Durr, Opt. Comm. 36 (1981) 383.
[47] P.F. Moulton, IEEE J. Quant. Electron. QE 21 (1985) 1582.
[48] H. Manaa, R. Moncorgé, Opt. Quant. Electron. 22 (1990) S219–S226.
[49] H. Manaa, Y. Guyot, R. Moncorgé, Phys. Rev. B48 (1993) 3633.

[50] D. Welford, P.F. Moulton, Opt. Lett. 13 (1988) 975.
[51] N. Menyuk, D.K. Killinger, Appl. Opt. 26 (1987) 3061—3065.
[52] M.P. Frolov, Yu. P. Podmar'kov, Opt. Comm. 155 (1998) 313—316.
[53] P.F. Moulton, A. Mooradian, Appl. Phys. Lett. 35 (1979) 838.
[54] Z.M. Zhang, Y.B. Cui, F.L. Li, G.B. Zhang, Q.R. Pu, G.J. Xu, Appl. Opt. 41 (6) (2002) 1071.
[55] R. Pappalardo, D.L. Wood, R.C. Linares, J. Chem. Phys. 35 (1961) 2041.
[56] H.A. Weakliem, J. Chem. Phys. 36 (1962) 2117.
[57] J. Ferguson, D.L. Wood, L.G. Van Uitert, J. Chem. Phys. 51 (1969) 2904.
[58] D.L. Wood, J.P. Remeika, J. Chem. Phys. 46 (1967) 3595.
[59] J.M. Baranowski, J.W. Allen, G.L. Pearson, Phys. Rev. 160 (1967) 627—632.
[60] D.S. McClure, J. Chem. Phys. 36 (1962) 2757.
[61] Y. Tanabe, S. Sugano, J. Phys. Soc. Jap. 9 (1954) 753.
[62] M. Avinor, G. Meijer, J. Phys. Chem. Sol. 12 (1960) 211.
[63] J.W. Allen, Physica 29 (1963) 764.
[64] G.A. Slack, B.M. O'Meara, Phys. Rev. 163 (1961) 335—341.
[65] G.A. Slack, F.S. Ham, R.M. Chrenko, Phys. Rev. 152 (1966) 376—402.
[66] J.T. Vallin, G.A. Slack, S. Roberts, A.E. Hughes, Phys. Rev. B2 (1970) 4313—4333.
[67] H. Nelkowski, G. Grebe, J. Lumin. 1—2 (1970) 88—93.
[68] V. Petricevic, S.K. Gayen, R.R. Alfano, Appl. Phys. Lett. 52 (13) (1988) 1040.
[69] N.B. Angert, N.I. Borodin, V.M. Garmash, V.A. Zhitnyuk, A.G. Okhrimchuk, O.G. Siyuchenko, A.V. Shestakov, Sov. Phys. Quant. Electron. 18 (1) (1988) 73.
[70] L.D. DeLoach, R.H. Page, G.D. Wilke, S.A. Payne, W.F. Krupke, IEEEE J. Quant. Electron. QE 32 (1996) 885—895.
[71] R.H. Page, K.I. Schaffers, L.D. DeLoach, G.D. Wilke, F.D. Patel, J.B. Tassano Jr., S.A. Payne, W.F. Krupke, K.T. Chen, A. Burger, IEEE J. Quant. Electron. QE 33 (1997) 609—619.
[72] J.J. Adams, C. Bibeau, R.H. Page, S.A. Payne, in: M.J. Fejer, H. Injeyan, U. Keller (Eds.), OSA TOPS, vol. 26, ASSL, 1999, p. p 435.
[73] J.J. Adams, C. Bibeau, R.H. Page, S.A. Payne, in: M.M. Fejer, H. Injeyan, U. Keller (Eds.), OSA TOPS, vol. 26, ASSL, 1999, pp. 435—440.
[74] J. Kernal, V.V. Fedorov, A. Gallian, S.B. Mirov, V.V. Badikov, Opt. Expr. 13 (26) (2005) 10608—10615.
[75] V.V. Fedorov, S.B. Mirov, A. Gallian, D.V. Badikov, M.P. Frolov, Y.V. Korostelin, V.I. Kozlovski, A.I. Landman, Y.P. Podmer'kov, V.A. Akimov, A.A. Voronov, IEEE J. Quant. Electron. 42 (9) (2006) 907—917.
[76] V. Petricevic, S.K. Gayen, R.R. Alfano, in: M.L. Shand, M.P. Jenssen (Eds.), Proceed. OSA Proc. On TSSL, vol. 5, 1989, p. 77.
[77] R. Moncorgé, G. Cormier, D.J. Simkin, J.A. Capobianco, OSA Proc. On TSSL 1989, vol. 5, p 60, eds M.L. Shand, M.P. Jenssen, and IEEE J. Quant. Electron. 27(1) (1991) 114.
[78] W. Jia, H. Liu, S. Jaffe, W.M. Yen, B. Denker, Phys. Rev. B43 (7) (1991) 5234.
[79] G.M. Zverev, A.V. Shestakov, in: M.L. Shand, M.P. Jenssen (Eds.), OSA Proc. On TSSL, vol. 5, 1989, p. 66.
[80] S. Kück, K. Petermann, G. Huber, in: G. Dubé, L. Chase (Eds.), OSA Proc. On ASSL, vol. 10, 1991, p. 92.
[81] H. Eilers, K.R. Hoffman, W.M. Dennis, S.M. Jacobsen, W.M. Yen, Appl. Phys. Lett. 61 (25) (1992) 2958.
[82] M.H. Garrett, V.H. Chan, H.P. Jenssen, W.H. Whitmore, A. Sacra, D.J. Singel, in: G. Dubé, L. Chase (Eds.), OSA Proc. On ASSL, vol. 10, 1991, p. 76.
[83] W. Jia, H. Liu, S. Jaffe, W.M. Yen, B. Denker, Phys. Rev. B 43 (7) (1991) 5234—5242.
[84] S. Kück, U. Pohlmann, K. Petermann, G. Huber, T. Schönherr, J. Lumin. 60&61 (1994) 192—196.
[85] H. Eilers, U. Hommerich, S.M. Jacobsen, W.M. Yen, K.R. Hoffman, W. Jia, Phys. Rev. B 49 (1994) 15505.
[86] K.R. Hoffman, U. Hömmerich, S.M. Jacobsen, W.M. Yen, J. Lumin. 52 (1992) 277—279.
[87] A. Sennaroglu, C.R. Pollock, H. Nathel, J. Opt. Soc. Am. B 12 (5) (1995) 930.
[88] S. Kück, K. Petermann, U. Pohlmann, U. Schönhoff, G. Huber, Appl. Phys. B58 (1994) 153.
[89] R. Moncorgé et, H. Manaa, Ann. Chim. 20 (1995) 241—248.
[90] R. Moncorgé, H. Manaa, G. Boulon, Opt. Mater. 4 (1994) 139—151.
[91] R. Moncorgé, H. Manaa, F. Deghoul, C. Borel, Ch. Wyon, Opt. Comm. 116 (1995) 393—397.
[92] N.V. Kuleshov, V.P. Mikhailov, V.G. Scherbitsky, B.I. Minkov, T.J. Glynn, R. Sherlock, Opt. Mater. 4 (1995) 507—513.
[93] C. Deka, B.H.T. Chai, Y. Shimony, X.X. Zhang, E. Munin, M. Bass, Appl. Phys. Lett. 61 (18) (1992) 2141.
[94] R. Moncorgé, H. Manaa, A.A. Kaminskii, Chem. Phys. Lett. 200 (6) (1992) 63.
[95] F. Deghoul, H. Chermette, F. Rogemond, R. Moncorgé, C. Stückl, C. Daul, Phys. Rev. B60 (1999) 2404—2409.
[96] V. Petricevic, A.B. Bykov, J.M. Evans, R.R. Alfano, Opt. Lett. 21 (1996) 1750.
[97] V. Petricevic, A.B. Bykov, J.M. Evans, A. Seas, A. Delgado, R.R. Alfano, G.V. Kanunnikov, in: Conf. Lasers Electro-optics, Tech. Dig., Baltimore, 1997 (Opt. Soc. Am., Washington 1997) CTuE7.
[98] N. Zhavoronkov, A. Avtukh, V. Mikhailov, Appl. Opt. 36 (1997) 8601.
[99] A.V. Shestakov, N.I. Borodin, V.A. Zhitnyuk, A.G. Okhrimchuk, V.P. Gaponstev, in: Conference on Lasers and Electro-optics, Vol. 10 of 1991 OSA Tech. Dig. Series, Optical Society of America, Washington, D.C., 1991 postdeadline paper CPDP 11—1.
[100] X. Eilers, W.M. Dennis, W.M. Yen, S. Kück, K. Petermann, G. Huber, W. Jia, IEEE J. Quant. Electron. 29 (1993) 2508.
[101] V. Yanovsky, Y. Pang, F. Wise, B.I. Minkov, Opt. Lett. 18 (1993) 1541.
[102] C. Chudoba, J.G. Fujimoto, E.P. Ippen, H.A. Haus, U. Morgner, F.X. Kärtner, V. Scheuer, G. Angelow, T. Tschudi, Opt. Lett. 26 (2001) 292.
[103] Y.P. Tong, J.M. Sutherland, P.M.W. French, J.R. Taylor, A.V. Shestakov, B.H.T. Chai, Opt. Lett. 21 (1996) 644.
[104] H. Manaa, Y. Guyot, F. Deghoul, R. Moncorgé, Chem. Phys. Lett. 238 (1995) 333—337.
[105] W.F. Krupke, R.H. Page, K.I. Schaffers, S.A. Payne, R.J. Beach, J.A. Skidmore, M.A. Emanuel, in: SPIE, vol. 3176, 1997, p. 47.
[106] S. Kück, J. All. Comp 341 (2002) 28—33.
[107] N. Tolstik, E. Sorokin, I. Sorokina, Opt. Lett. 38 (3) (2013) 299—301.
[108] D.M. Andrauskas, Ch. Kennedy, in: G. Dubé, L. Chase (Eds.), OSA Proc. On ASSL, vol. 10, 1991, p. 393.
[109] R. Moncorgé, H. Manaa, F. Deghoul, Y. Guyot, Y. Kalisky, S.A. Pollack, E.V. Zharikov, M. Kokta, Opt. Comm. 132 (1996) 279.
[110] K.V. Yumashev, N.N. Posnov, I.A. Denisov, V.P. Mikhailov, R. Moncorgé, J. Opt. Soc. Am. B15 (1998) 1707—1713.
[111] I.A. Denisov, K.V. Yumashev, R. Moncorgé, B. Ferrand, Appl. Opt. 40 (2001) 5413—5416.
[112] A.M. Malyarevich, I.A. Denisov, K.V. Yumashev, V.P. Mikhailov, R.S. Conroy, B.D. Sinclair, Appl. Phys. B 67 (1998) 555—558.
[113] D.P. Jiang, Y.Q. Zou, L.B. Su, H.L. Tang, F. Wu, L.H. Zheng, H.J. Li, J. Xu, Laser Phys. Lett. 8 (2011) 343—348.
[114] K.V. Yumashev, I.A. Denisov, N.N. Posnov, V.P. Mikhailov, R. Moncorgé, D. Vivien, E. Ferrand, Y. Guyot, J. Opt. Soc. Am. B16 (1999) 2189—2194.
[115] K.V. Yumashev, I.A. Denisov, N.N. Posnov, N.V. Kuleshov, R. Moncorgé, J. All. Comp. 341 (2002) 366—370.
[116] V.G. Shcherbitsky, S. Girard, M. Fromager, R. Moncorgé, N.V. Kuleshov, V.I. Levchenko, V.N. Yakimovich, B. Ferrand, Appl. Phys. B 74 (2002) 367—374.
[117] A. Podlipensky, V.G. Shcherbitsky, M.I. Demchuk, N.V. Kuleshov, V.I. Levchenko, V.N. Yakimovich, S. Girard, R. Moncorgé, Opt. Comm. 192 (1—2) (2001) 65—68.
[118] V.I. Kalashnikov, V.G. Shcherbitsky, N.V. Kuleshov, S. Girard, R. Moncorgé, Appl. Phys. B 75 (2002) 35—39.
[119] M. Laroche, A. Chardon, J. Nilsson, D.P. Shepherd, W.A. Clarkson, S. Girard, R. Moncorgé, Opt. Lett. 27 (2002) 1980—1982.
[120] T.Y. Tsai, M. Birnbaum, Appl. Opt. 40 (36) (2001) 6633—6637.